An Iterative Electro-Thermal Model for An Active Antenna Element and Its Application to Arrays

Feza Turgay Celik[#], Christian Fager[$], Alexander Yarovoy[#], Yanki Aslan[#]

[#]Delft University of Technology, The Netherlands
[$]Chalmers University of Technology, Sweden
{f.t.celik, a.yarovoy, y.aslan}@tudelft.nl, christian.fager@chalmers.se

***Abstract*— A novel electro-thermal model at the unit-cell level for active phased arrays is proposed to establish a link between the power amplifier (PA) output signal and its junction temperature. The iterative model is developed in four stages: (i) calculation of the PA output, (ii) computation of the dissipated power of the PA, (iii) thermal simulation for temperature assessment, and (iv) update on the PA output with the new temperature. These steps are repeated until the PA temperature is convergent. The use of the model is demonstrated with an amplitude-tapered 16-element array of single-stage class-A amplifier and patch antenna unit-cells at 2.14 GHz. It is observed that the inclusion of the temperature effects in the array pattern causes around a 2 dB drop in the radiated power, while the peak side lobe level (SLL) increases by up to 7.75 dB for 40 dB Taylor tapering.**

***Keywords*— active antennas, beamforming, calibration, electro-thermal characterization, phased arrays, side lobes.**

I. Introduction

Active phased arrays with close integration of beamforming electronics and antennas enable modern communication and sensing applications [1], [2]. However, the large power density of the power amplifiers (PAs) [3] brings significant challenges in thermal management both in sub-6 GHz and millimeter-wave bands [4], and array calibration becomes more complex due to temperature non-uniformities across the array [5].

In many applications, the array radiation patterns must adhere to the standards set by regulatory organizations such as ITU and ETSI [6]. This means that the side lobe levels should remain within the limits specified by a particular mask in transmit mode, which is enabled by amplitude tapering [7]. Amplitude tapering is achieved by modifying the output power delivered by each PA, which has an impact on its power dissipation [8]. The dissipated heat raises the temperature of the PA and causes a change in the output power. This iterative electro-thermal coupling mechanism may lead to significant distortions in the array pattern at the steady-state. In turn, the side lobe requirements on the radiation pattern mask may be violated. Therefore, understanding the temperature dependence of side lobe levels, and calibrating out the errors in the pattern masks is an important problem that is yet to be resolved.

Several electro-thermal analysis approaches have been proposed in the literature. Detailed electro-thermo-mechanical modeling (e.g. via the finite element method, FEM) [9] is accurate yet too complex for array synthesis problems for which the search space is too large. On the other hand, the studies that link the temperature effects on the component material properties [10] (via losses, thermal expansion coefficients etc.) do not reflect the physical changes on the PA signals. The electro-thermal behavioral models proposed in [11], [12] were developed to characterize the temperature-dependent effects of PA signals. However, the link to pattern side lobe requirements, assessment and effects of varying temperature distribution across the array, and impacts of calibration for pattern mask compensation were not studied.

In this paper, a new iterative electro-thermal model of an integrated PA-antenna unit cell is proposed. PA dissipated power and output signals are modeled and updated based on the outcome of the thermal simulations of active patch antennas. Various amplitude-tapering scenarios are discussed, and the negative impact of the temperature increase and non-uniformities on the pre-defined side lobe level masks are illustrated for the first time. Moreover, the effects of calibrating out the side lobe errors are discussed.

The rest of the paper is organized as follows. Section II describes the electro-thermal model. Section III discusses the simulation results. Section IV concludes the paper.

II. Electro-Thermal Model of a Unit-Cell

A phased array unit-cell (single PA + antenna element) level iterative electro-thermal model is proposed in this section. The model is developed under the following assumptions:

- Each PA is connected to a single antenna.
- Power is computed for continuous wave (CW) operation.
- Steady-state condition is considered.
- There is no thermal or electromagnetic coupling between the neighboring unit cells.

The iterative electro-thermal model can be seen in Fig. 1.

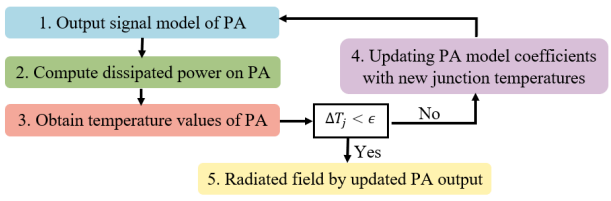

Fig. 1. Flow diagram representation of the proposed electro-thermal model.

The model starts with the computation of the power waves generated by the PA. A complex envelope polynomial

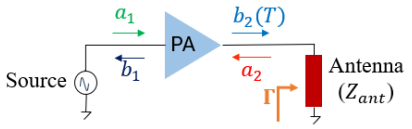

Fig. 2. Circuit diagram of a unit cell and power waves.

expansion expresses the output wave in terms of input and reflection parameters. In the second step, the power dissipated by the transistor in PA, P_{diss}, is calculated. In step 3, thermal simulations are performed by considering P_{diss} as a volumetric heat source, and the polyharmonic expansion coefficients in the PA signal model is updated with the new temperature. This procedure is repeated in step 4 until convergence (i.e. when the PA junction temperature between two iterations become less than 0.25^0C). Finally, in step 5, with the new PA output and radiated power of each unit cell, a realistic array factor is formulated. Next, further details on each step are given.

A. *Signal Model of the PA*

The input power wave to the PA (a_1) and the reflected power wave from an antenna element (a_2) are used to calculate the output power wave of the PA (b_2). The wave a_2 can be represented with the reflection coefficient of the antenna (Γ) and b_2 for compactness. See Fig. 2 for the signal visualization.

The quasi-static polynomial expansion model formulates the b_2 wave [12] as weighted sums of a_1, a_2, and $(a_1)^2a_2^*$, as;

$$b_2[n] = \sum_{k=1}^{K} \alpha_k a_1[n]|a_1[n]|^{2(k-1)} + \sum_{k=1}^{K} \beta_k a_2[n]|a_1[n]|^{2(k-1)} + \sum_{k=2}^{K} \gamma_k (a_1[n])^2 a_2^*[n]|a_1[n]|^{2(k-2)} \quad (1)$$

The expansion illustrated in (1) is converted to the format of $b_2 = A\phi$, where $\phi = [\alpha(T); \beta(T); \gamma(T)]$. The coefficient vector (ϕ) is temperature dependent and can be calculated by applying the least mean squares method on a large data set generated in the ADS environment. In this work, a simple class-A amplifier with the MACOM CGH40010 transistor package is used at a 2.14 GHz operation frequency for demonstration. The schematic of the ADS setup can be seen in Fig. 3. The model of the b_2 becomes more accurate with increased order of expansions; however, numerical errors dominate in the non-linear region of the PA and yield significant errors for a large K. This can be seen by inspecting the variation of b_2 and the gain value of the PA with respect to K in Fig.4. Based on this study, K is set to 6.

B. *Dissipated Power Model of the PA*

The dissipated power of the PA depends on the RF input power, RF output power, and DC power. The RF input power can directly be characterized by a_1. Similarly, RF output power can be described with b_2 and Γ. However, modeling DC power using power waves is not as simple as the RF power. Here, we use power series expansion with the $|b_2[n]|^2$ terms. The corresponding power relations are formulated in (2) - (5).

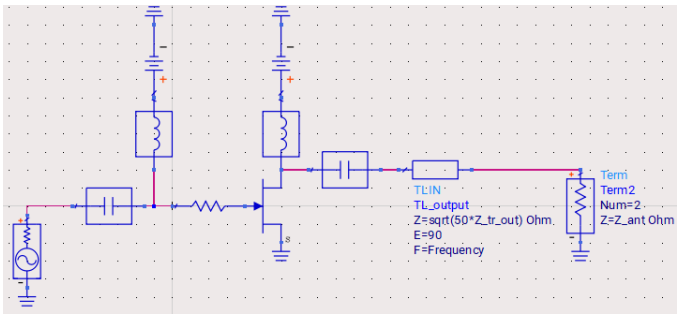

Fig. 3. ADS circuit model of the single-stage class-A amplifier.

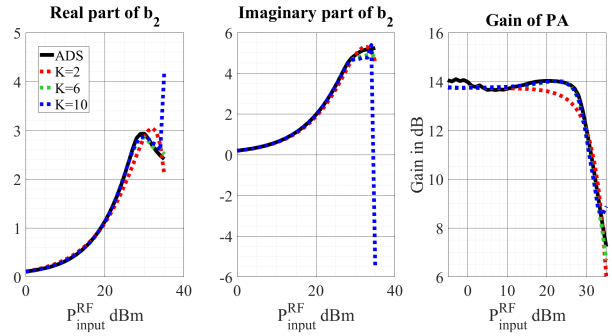

Fig. 4. Comparison of modeled and simulated b_2 and gain values of the PA.

$$P_{diss} = R_{RF}^{in} + P_{DC} - P_{RF}^{out} \quad (2)$$

$$P_{RF}^{in} = |a_1|^2/2 \quad (3)$$

$$P_{RF}^{out} = |b_2|^2 Real((1+\Gamma)(1-\Gamma))/2 \quad (4)$$

$$P_{DC} = \sum_{p=1}^{P} \psi_p |b_2|^{2(p-1)} \quad (5)$$

The coefficients (ψ_p) for the power series are obtained in a similar way to step 1, and P is set to 6.

C. *Thermal Model of the Unit Cell*

The dissipated power in the PA is the input of the thermal simulation of the system. We use a finite element-based solver (ANSYS Mechanical) to compute the junction temperature of a packaged PA. A side view of the thermal simulation environment can be seen in Fig. 5. The open air boundaries are defined as convection boundaries with a fixed heat transfer coefficient of 10 W/m^{2}K to impose a stationary air condition.

The model consists of a square patch antenna (of 35.6 mm length), a dielectric (Rogers 4003, ϵ_r= 3.55, with 1.6 mm thickness), a ground plate, and a heat source. The heat source is modeled with the standard two-resistor approach, represented by a junction-to-board resistance, R_{jb} = 14 K/W and junction-to-case resistance, R_{jc} = 10 K/W [13]. Conventionally, the PA is cooled down by a large heatsink [4]. Depending on the heatsink size, the power of the heat

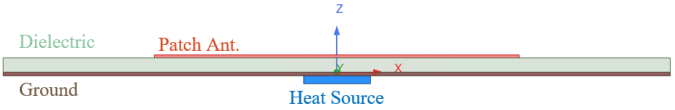

Fig. 5. The side view of the thermal FEM model in ANSYS Mechanical.

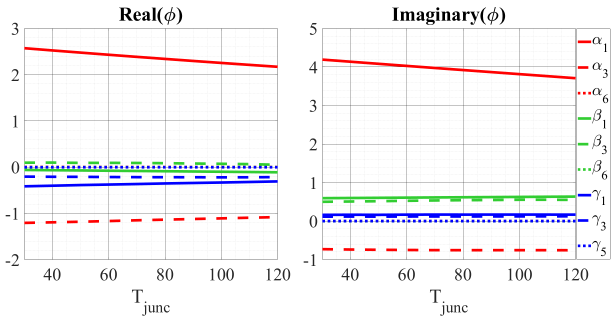

Fig. 6. Variation in the α, β, and γ coefficients of different orders.

source, P_{diss} can be scaled by the power scaling factor $\zeta \leq 1$. No heatsink means $\zeta = 1$, leading to the highest temperature.

D. Updating the Coefficients in the Polynomial Expansion

The behavior of the transistor is measured and formulated by the manufacturer. Each coefficient (ϕ) of the polynomial expansion is affected by the temperature. As shown in Fig. 6, the variation of the coefficients changes linearly with respect to the PA junction temperature, T_{junc}. Therefore, linear equations are used to update the coefficients in step 4, based on the temperatures in step 3, until the convergence is reached.

III. Simulation Results

A. Unit-Cell Results

The proposed model converges in 3 to 4 iterations. The convergence of T_{junc} for different input power values can be seen in Fig. 7. Two major observations are made regarding the relation between the increase in the T_{junc} of the PA and the output signal (b_2) of the PA:

1) Increase in the T_{junc} yields a drop in the $|b_2|$, causing a drop in the power of the amplified signal.
2) The more the PA heats up, the more change will be seen in the b_2. In other words, the signal distortion is not uniform with respect to the temperature changes.

Let us define the output power of a PA when it is working at the ambient temperature of 20^oC as P_{out}^{Ideal}, which serves as the initial condition in our iterative model. The changes introduced by the proposed model can be seen best by investigating the behavior of P_{out}^{Ideal} and P_{out}^{ζ} values and their ratios in Fig. 8. T_{junc} values corresponding to different ζ values are 55.1^oC, 125.6^oC, and 231.7^oC for $\zeta = 0.06$, 0.18, and 0.36. It is observed that the temperature correction has a more dramatic effect on higher input powers. Also, the

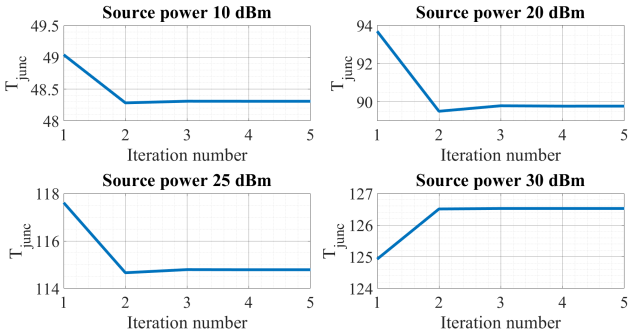

Fig. 7. T_{junc} vs. iterration number for different input power values.

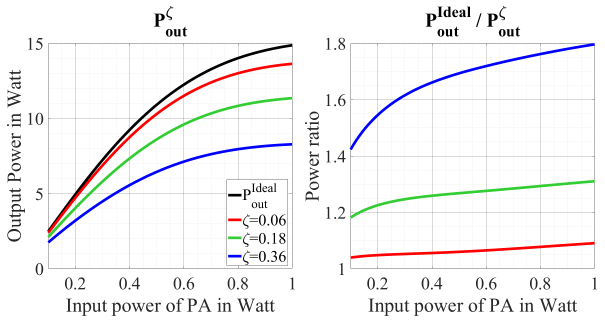

Fig. 8. PA output power values for different ζ (left). The power ratio between P_{out}^{Ideal} and P_{out}^{ζ} for different ζ values (right).

change in the output power is more significant in higher ζ values. These observations highlight that a greater increase in T_{junc} means a greater reduction in P_{out}.

B. Array Results

The main purpose of the electro-thermal model is to observe the changes in the radiation pattern and the delivered power in the array structures considering the heating of PAs when there is amplitude tapering. The unit-cell scale PA output signals are used as inputs in the full-wave simulations at the antenna array scale. We consider a 16-element linear array of coax probe-fed patch antennas at 2.14 GHz. Three different Taylor-windowed amplitude taperings are investigated for -20, -30, and -40 dB SLL. The maximum input power of the PA is set to 27 dBm as this operating point is close to the limit of the stationary gain of the PA. The radiation patterns of the -20, -30, and -40 dB SLL Taylor tapered arrays at $\phi = 90^0$ cut can be seen in Fig. 9 for the broadside radiation of the array. The detailed analysis of temperature effects on SLL in different scan angles is provided in Table 1.

As observed in Fig. 9, the distortion in the SLL is more dominant in the -40 dB Taylor windowing, as the power ratios between the antenna elements are larger. In addition, the radiation pattern is more distorted when ζ increases. This outcome highlights that the more the transistor heats up, the more relative change is observed in its output. The distortion in the radiation pattern is not the only change that occurs due to the increase in transistor temperatures. The maximum radiated power also changes with temperature. The incident, accepted,

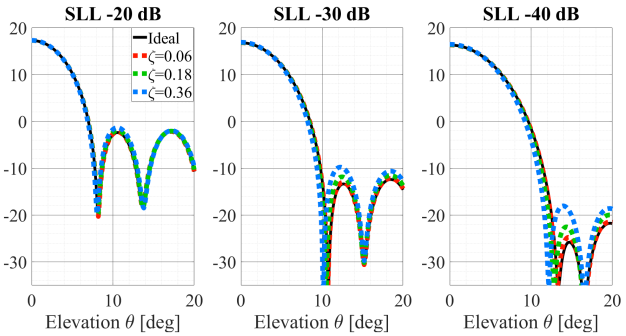

Fig. 9. Radiation pattern of the broadside pattern for -20, -30, and -40 dB SLL Taylor window excitations in a 16-element active patch array for different ζ values.

Table 1. Simulated peak SLL [dB] of different Taylor excitations in a 16-element linear active patch array for ideal, ζ = 0.06, 0.18, and 0.36 cases in $\theta = 0^o$, 30^o, 45^o, and 60^o main beam directions.

Beam	SLL -20 dB Taylor Excitation				SLL -30 dB Taylor Excitation				SLL -40 dB Taylor Excitation			
Direction	Ideal	ζ = 0.06	ζ = 0.18	ζ = 0.36	Ideal	ζ = 0.06	ζ = 0.18	ζ = 0.36	Ideal	ζ = 0.06	ζ = 0.18	ζ = 0.36
$\theta = 0^o$	-19.68	-19.55	-19.26	-18.62	-30.24	-29.87	-28.72	-26.64	-42.22	-41.17	-38.96	-34.47
$\theta = 30^o$	-19.79	-19.66	-19.37	-18.72	-30.39	-30	-28.89	-26.79	-39.29	-38.58	-37.07	-33.47
$\theta = 45^o$	-18.84	-18.72	-18.46	-17.84	-29.95	-29.58	-28.39	-26.27	-39.81	-39.17	-37.64	-33.78
$\theta = 60^o$	-17.28	-17.16	-16.91	-16.32	-27.3	-26.96	-25.92	-24.03	-39.75	-38.68	-36.18	-32.09

Table 2. Incident, accepted and radiated power [dB, normalized] by the 16 element array for SLL -20, -30, -40 dB Taylor excitations considering ideal, ζ = 0.06 , 0.18, and 0.36 thermal conditions.

Tapering Type	Ant. Power	Ideal	ζ=0.06	ζ=0.18	ζ=0.36
Uniform (no tapering)	Incident	0	-0.25	-1.03	-2.29
	Accepted	-0.4	-0.65	-1.43	-2.69
	Radiated	-1.05	-1.3	-2.09	-3.34
Taylor Tapering SLL = -20 dB	Incident	-1.7	-1.93	-2.67	-3.82
	Accepted	-2.14	-2.37	-3.12	-4.27
	Radiated	-2.91	-3.14	-3.88	-5.03
Taylor Tapering SLL = -30 dB	Incident	-3.07	-3.3	-4.02	-5.13
	Accepted	-3.54	-3.76	-4.48	-5.59
	Radiated	-4.31	-4.53	-5.25	-6.36
Taylor Tapering SLL = -40 dB	Incident	-3.72	-3.94	-4.66	-5.77
	Accepted	-4.19	-4.41	-5.13	-6.24
	Radiated	-4.96	-5.18	-5.9	-7.01

and radiated power values of the array are provided for each excitation case for different cooling ratios in Table 2. In this table, the incident power in uniform feeding (10.93 W per PA) and idealized cooling conditions (for ambient temperature in PAs) is used as a reference (= 0 dB), and the rest are calculated accordingly. It is seen that the heating of the PA reduces its output power, resulting in low incident power for the antenna. Radiated power also reduces if the constraints on the SLL are made more strict, as expected due to the lower input power of the edge elements with tapering.

IV. Conclusion

A unit-cell (a single PA and antenna) level iterative electro-thermal model is proposed to formulate the changes of the PA output signals with respect to the PA junction temperature at steady-state. The model creates a loop between the PA dissipated power and temperature of the PA through thermal simulations. A class-A amplifier with a patch antenna at 2.14 GHz is used for model demonstration. It is observed that the temperature effects become dominant for high input power and poor external cooling conditions. Furthermore, the impact of the thermal correction on the PA output signals, and thus on the phased array pattern side lobes is illustrated through amplitude tapering. Different Taylor excitation schemes are studied, and it is observed that ignoring thermal effects results in SLL errors, which increase with the tapering level and go up to 7.75 dB for -40 dB SLL. The proposed model provides reliable SLL assessment in array synthesis and is adaptable to various PA and antenna types. Future work in modeling will focus on the electro-thermal coupling between the unit cells.

Acknowledgment

This research was supported by the National Growth Fund through the Dutch 6G flagship project "Future Network Services". The authors also thank the European Microwave Association for enabling this joint research with the EuMA Internship Award.

References

[1] K. K. W. Low, S. Zihir, T. Kanar, and G. M. Rebeiz, "A 27–31-ghz 1024-element ka-band satcom phased-array transmitter with 49.5-dbw peak eirp, 1-db ar, and ±70° beam scanning," *IEEE Transactions on Microwave Theory and Techniques*, vol. 70, no. 3, pp. 1757–1768, 2022.

[2] R. D. Palmer *et al.*, "Horus—a fully digital polarimetric phased array radar for next-generation weather observations," *IEEE Transactions on Radar Systems*, vol. 1, pp. 96–117, 2023.

[3] B. Sadhu, X. Gu, and A. Valdes-Garcia, "The more (antennas), the merrier: A survey of silicon-based mm-wave phased arrays using multi-ic scaling," *IEEE Microwave Magazine*, vol. 20, no. 12, pp. 32–50, 2019.

[4] Y. Aslan, J. Puskely, J. H. J. Janssen, M. Geurts, A. Roederer, and A. Yarovoy, "Thermal-aware synthesis of 5g base station antenna arrays: An overview and a sparsity-based approach," *IEEE Access*, vol. 6, pp. 58 868–58 882, 2018.

[5] Y. Aslan, P. Aubry, N. B. Onat, J. Janssen, M. Geurts, and A. Yarovoy, "Heuristic over-the-air calibration of beamformer ics in active mm-wave phased arrays," in *2023 IEEE Conference on Antenna Measurements and Applications (CAMA)*, 2023, pp. 840–845.

[6] A. Haddadi, E. Alfonso, C. Bencivenni, and T. Emanuelsson, "E-band high gain gap waveguide slot array antenna with etsi class-iii radiation pattern suitable for mass production," in *2018 IEEE International Symposium on Antennas and Propagation USNC/URSI National Radio Science Meeting*, 2018, pp. 1103–1104.

[7] T. Taylor, "Design of line-source antennas for narrow beamwidth and low side lobes," *Transactions of the IRE Professional Group on Antennas and Propagation*, vol. 3, no. 1, pp. 16–28, 1955.

[8] E. McCune, "Foundations of green communications," in *2015 IEEE International Conference on Communication Workshop (ICCW)*, 2015, pp. 2744–2749.

[9] H. H. Zhang, X. Y. Liu, Y. Liu, Z. C. Fan, and H. L. Du, "Thermal-mechanical-electromagnetic multiphysics simulation of satellite phased array antenna based on dgtd and fem method," *IEEE Journal on Multiscale and Multiphysics Computational Techniques*, vol. 9, pp. 236–246, 2024.

[10] H.-X. Zhang, L. Huang, W.-J. Wang, Z.-G. Zhao, L. Zhou, W. Chen, H. Zhou, Q. Zhan, B. Kolundzija, and W.-Y. Yin, "Massively parallel electromagnetic–thermal cosimulation of large antenna arrays," *IEEE Antennas and Wireless Propagation Letters*, vol. 19, no. 9, pp. 1551–1555, 2020.

[11] P. Taghikhani, K. Buisman, M. Versleijen, J.-R. Perez-Cisneros, and C. Fager, "Temperature-dependent characterization of power amplifiers using an efficient electrothermal analysis technique," *IEEE Transactions on Microwave Theory and Techniques*, vol. 70, no. 2, pp. 1349–1360, 2022.

[12] C. Fager, K. Hausmair, T. Eriksson, and K. Buisman, "Analysis of thermal effects in active antenna array transmitters using a combined em/circuit/thermal simulation technique," in *2015 Integrated Nonlinear Microwave and Millimetre-wave Circuits Workshop (INMMiC)*, 2015, pp. 1–3.

[13] F. T. Celik, A. Yarovoy, and Y. Aslan, "From cooling to coupling and back: A novel beam- switching heatsink antenna array with csrr embedded isolation wall," *IEEE Antennas and Wireless Propagation Letters*, vol. 22, no. 11, pp. 2690–2694, 2023.